

PAPER

Numerical simulation of an atmospheric pressure plasma jet with coaxial shielding gas

To cite this article: Peng Lin *et al* 2021 *J. Phys. D: Appl. Phys.* **54** 075205

View the [article online](#) for updates and enhancements.



IOP | ebooks™

Bringing together innovative digital publishing with leading authors from the global scientific community.

Start exploring the collection—download the first chapter of every title for free.

Numerical simulation of an atmospheric pressure plasma jet with coaxial shielding gas

Peng Lin¹ , Jiao Zhang² , Tam Nguyen¹ , Vincent M Donnelly¹ 
and Demetre J Economou¹ 

¹ Plasma Processing Laboratory, Department of Chemical and Biomolecular Engineering, University of Houston, Houston, TX 77204, United States of America

² On leave from School of Physics, Dalian University of Technology, Dalian 116024, People's Republic of China

E-mail: vmdonnelly@uh.edu and economou@uh.edu

Received 28 June 2020, revised 24 September 2020

Accepted for publication 20 October 2020

Published 30 November 2020



CrossMark

Abstract

A two-dimensional (r, z) numerical simulation of the discharge characteristics of an atmospheric pressure plasma jet (APPJ), with coaxial shielding gas, was performed. The helium working gas flowed in a central capillary tube, engulfing a needle electrode powered by 13.7 MHz radio frequency sinusoidal voltage. The N_2 shielding gas flowed in the annular space of a coaxial tube. These gases emerged, in laminar flow, in a 78% N_2 -21% O_2 -1%Ar dry air ambient. The characteristics of the APPJ with shielding gas were compared to those of the APPJ without shielding gas. The nitrogen shielding gas hindered the diffusion of oxygen and argon from the ambient air into the helium jet. With the shielding gas present, more nitrogen penetrated into the helium core, causing a shorter plasma 'plume'. The flow rates of the working and shielding gas, critically affected the gas temperature, and in turn the discharge characteristics. For a He flow of 2 standard liters per minute (slm), switching on the nitrogen shielding gas flow (at 4.5 slm) reduced the on-axis O_2 and Ar mole fractions from 3.9×10^{-4} to 6.8×10^{-5} and from 1.9×10^{-5} to 3.3×10^{-6} , respectively, at an axial distance of 3 mm downstream of the nozzle. The radial profiles of the mole fractions of the ambient gases were monotonically and strongly decreasing towards the system axis, for short axial distances from the nozzle (~ 1 mm), but became progressively flatter at longer distances from the nozzle (3 mm and 5 mm). Simulation predictions captured the salient features of experimental data of ambient species mole fractions in the plasma jet, and the 706 nm optical emission intensity profiles of the He 3^3S excited state.

Keywords: atmospheric pressure plasma jet, coaxial shielding gas, gas temperature distribution

(Some figures may appear in colour only in the online journal)

1. Introduction

Interest continues to increase in low-temperature (cold, non-equilibrium) atmospheric-pressure plasmas, fueled mainly by realized and potential biomedical [1–3], materials processing [4], and environmental [5] applications. For selected area exposure, the so-called atmospheric pressure plasma jet (APPJ) is most popular. A common configuration of APPJ entails flow of a working gas (most often He or Ar)

through a dielectric capillary tube, in which a plasma is sustained. The plasma 'plume' generally extends a few cm from the end of the tube (nozzle). The jet emanating from the nozzle naturally entrains ambient gas (usually open air), which mixes with the working gas resulting in a complex array of chemical reactions, that produce a plethora of reactive species. The composition of the open air ambient gas, however, is generally uncontrolled. For example, the amount of moisture (humidity) in the open air can change from day to day,

affecting the concentration of reactive species produced in the plasma jet [6]. One method to control the ambient gas is to enclose the system in a chamber flushed with a prescribed ambient gas composition. Such action, however, would limit the inherent portability and applications of the APPJ. A more compact design (figure 1, left) uses a coaxial tube providing an annular space where a gas of selected composition flows, forming a curtain that tends to shield the working gas from the ambient [7, 8]. An APPJ of coaxial shielding gas design has been marketed as kINPen [9].

The identity and flux of species delivered by an APPJ are important for applications. In particular, metastable species of He, Ar, and N₂ can profoundly affect the chemistry of the plasma. For example, He metastables play a significant role in Penning ionization of molecular gases, including N₂ and O₂ [10]. Also, N₂(A) metastables have relatively long effective lifetime, making them important in the late afterglow (power off) of pulsed discharges or far downstream of the nozzle in continuous wave APPJs [11]. Iseni *et al* [12] found that the highest N₂(A) concentration was achieved in the case of air admixtures in spite of the enhanced collisional quenching by O₂. Winter *et al* [7] measured the He(2³S₁) metastable density in an APPJ with a N₂/O₂ mixture as a shielding gas. The maximum metastable density was observed for a shielding gas with the composition of standard ambient air. When using pure oxygen as the shielding gas, the He metastable density decreased by 30%. When using pure nitrogen as the shielding gas, the metastable density was below the detection limit. Schmidt-Bleker *et al* [13] used a combination of measurements and a 0-D model to study reaction mechanisms in an Ar APPJ with varying shielding gas composition from pure N₂, to mixtures with O₂, to pure O₂. Yatom *et al* [14] studied a plasma jet fed with an Ar + 0.26% H₂O mixture and shielded by a coaxial argon flow to keep the water vapor concentration in the jet larger than that in the ambient air. Furthermore, Jablonowski *et al* [15] used a device with shielding gas to enhance the desired species concentration, thereby achieving greater rates of bacteria deactivation. Kapaldo *et al* [16] studied the effect of reactive species on cancer cells using a shielding-gas-controlled APPJ. Tresp *et al* [17] investigated the plasma chemistry with shielding gas composed of different mixtures of oxygen and nitrogen.

In a simulation study [8], the k- ϵ turbulent flow model was used to determine the concentration distribution of the feed gases and the ambient gas before plasma ignition. Sigeneer *et al* [18] simulated a reactor geometrically similar to that in the present work. However, in their work, the plasma was sustained in the annular space between the tubes (not in the central capillary tube). The plasma-activated gas reacted with the gas flowing through the central tube, immediately downstream of the nozzle before striking a substrate. A system involving multiple jets in 2-D cartesian (x , y) geometry was simulated by Babaeva *et al* [19] This system is also different than that of the present work since plasma was ignited in all conduits of the system. Finally, Schmidt-Bleker *et al* [20] examined the effect of composition of the shielding gas (N₂, O₂, and synthetic air) surrounding a He APPJ.

Despite the clear advantages of APPJ with coaxial shielding gas, relatively few simulation studies of this configuration have been reported in the literature. In particular, there is no systematic study of the behavior of an APPJ with a shielding gas as compared to the same APPJ without shielding gas. In the present work, a computational investigation of an APPJ with a coaxial shielding gas was conducted. The cases reported here used He, N₂ and dry air (78%N₂-21%O₂-1%Ar) as the working, shielding and ambient gas, respectively. Results were compared to an otherwise identical system but without shielding gas. Simulation predictions were also compared to experimental data in an APPJ reactor in our laboratory.

2. Simulation model

A schematic of the two-dimensional axisymmetric (r , z) coaxial jet system studied is shown in figure 1 (left panel). The system consisted of two coaxial dielectric (quartz) capillary tubes. The helium working gas flowed through the central tube (base case of 2 standard liters per minute, slm), while the nitrogen shielding gas (base case 4.5 slm) flowed in the annular space between the tubes. The ID (inside diameter) and OD (outside diameter) of the central tube were 2 mm and 3 mm, respectively. The coaxial tube had an ID = 6 mm and an OD = 8 mm. A metal needle electrode (1 mm diameter at the base), coaxial with the tubes, was used to power the discharge with a 2 kV peak-to-peak sinusoidal voltage waveform at 13.7 MHz. The tip of the needle electrode (with a 350 μ m radius of curvature), was 3 mm upstream of the nozzle. A metal sheet (axial length 11 mm), was wrapped around the outside wall of the central tube, and served as the grounded electrode. The upper edge of this electrode was at the same axial location as the tip of the needle.

The simulation consisted of two parts: a neutral gas convective mass and heat transport model (without chemical reactions), and a plasma dynamics model with plasma chemical reactions, involving neutrals, positive and negative ions, as well as electrons. The larger domain (AMNOA) in figure 1 (middle panel) was used for the neutral gas model, while the smaller domain (QRSOQ) in figure 1 (right panel) was used for the plasma model. The extend of the computational domain is a compromise between large enough domain size for more realistic simulation, and small enough domain size for reasonable computational burden. In the present work, the domain size was chosen so that the experimentally observed ‘plume’ of the plasma jet fit comfortably in the simulation domain.

The helium working gas flowed through the central dielectric tube with a flow rate (Q) ranging from 1.0 slm to 5.0 slm, corresponding to an average gas flow velocity (at 1 atm and 300 K) of 7.8 m s⁻¹ to 39 m s⁻¹ (based on the cross sectional area between the needle base and the inner wall of the central tube). The nitrogen shielding gas flowed in the annular space between the tubes, with a flow rate ranging from 4.5 slm to 9.0 slm (average velocity of 5.25 m s⁻¹ to 10.5 m s⁻¹). The Reynolds number was calculated by $Re = u\rho d/\mu$, where u , ρ , and μ are the average flow velocity, density, and viscosity of the gas, respectively, and d is a characteristic length scale

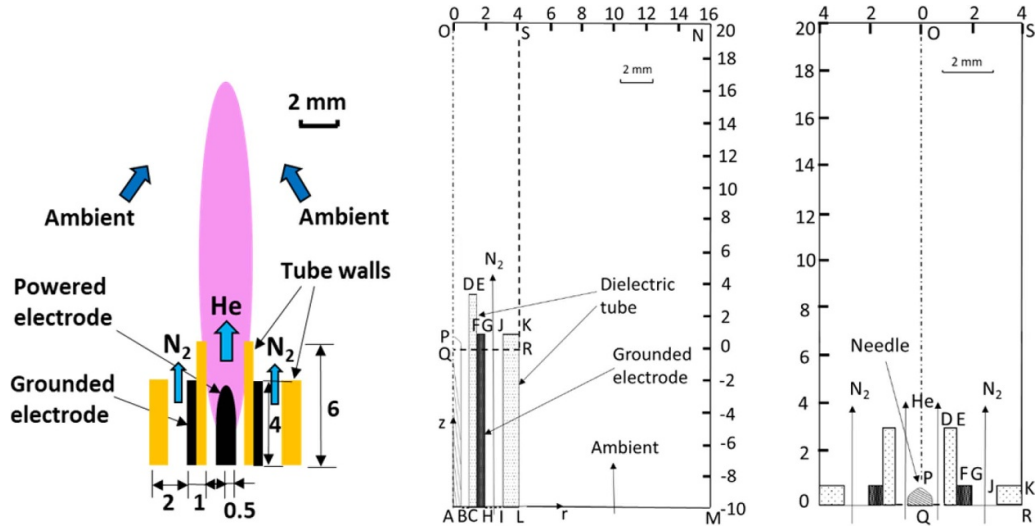


Figure 1. (left panel, units are in mm): Schematic of a He APPJ with coaxial shielding gas (N_2) flowing in the annular space. The helium working gas flows over the needle electrode through the central capillary tube. The shielding gas acts as a curtain that hinders mixing of ambient gas with the working He gas; (middle panel): schematic of neutral simulation domain AMNOA. Only ‘half’ of the domain is shown due to the axisymmetric nature of the problem, i.e. the left boundary is the axis of symmetry. Boundaries LM, MN and NO are open to the ambient. (right panel): plasma dynamics simulation domain. Only half of this domain (i.e. QRSOQ) was used for calculations. Base case conditions are He flow rate of 2 slm and nitrogen flow rate of 4.5 slm.

(e.g. the central tube inside diameter). The Reynolds number for the working gas ranged from 32 to 160, suggesting laminar flow. For the shielding gas, the Reynolds number ranged from 1100 to 2200, marginally in the laminar flow regime. It should be noted that the coaxial jet flow configuration is amenable to creation and propagation/growth of disturbances especially in the shear layer, at the interface between the two jets. This can cause the critical Reynolds number for transition from laminar to turbulent flow to be less than that for a single jet.

The species considered in the neutral gas convective mass and heat transport model were He, N_2 , O_2 and Ar. The species considered in the plasma dynamics model were He, $He(2^3S_1) = He^*$, $He_2(\alpha^3\Sigma_u) = He_2^*$, He^+ , He_2^+ , N_2 , N , $N_2(A^3\Sigma_u^+) = N_2(A)$, N_2^+ , O_2 , O , O_3 , O^- , O_2^- , O_2^+ , O_4^+ , NO, and electrons. The reaction mechanism used in the present work is shown in table 1. It consists of 101 reactions including electron impact ionization, excitation, de-excitation, dissociation, recombination, electron attachment, charge transfer, and Penning ionization [21]. The rate coefficients of electron impact reactions were calculated using a Maxwellian electron energy distribution function with cross-sections from the Phelps [22] and Trinity [23, 24] databases. Table 1 includes species that were not followed in the simulation, i.e. no mass balance equations were applied for these species. However, the reactions involving these species were accounted for in the electron energy balance equation, contributing to various channels of electron energy loss (or gain). Only the species shown on the list above were followed in the simulation. This is a common practice [25, 26] in order to reduce the computational burden, yet obtain a more accurate electron energy. Photoionization was not included in the simulation. According to Breden *et al* [27], photoionization is not needed to sustain the discharge, as long as an adequate background electron density exists ($\sim 10^8 \text{ cm}^{-3}$ or higher [28]). The secondary electron

emission coefficient due to ion bombardment of solid surfaces, γ_i , was taken as 0.01 for dielectrics and 0.1 for metals [29].

2.1. Neutral gas convective mass and heat transport model

This model predicted the 2-D steady-state gas velocity and temperature profiles and the mass (or mole) fraction distributions of the feed gases and the entrained ambient gas before plasma ignition, i.e. without chemical reactions. The total mass continuity equation (equation (1)), momentum conservation (Navier–Stokes) equations (equation (2)), species mass balance equations (equation (3)), and energy balance equation (equation (4)), were solved for the gas velocity field, mass fraction distribution of the neutral gases (He, N_2 , O_2 , Ar) and neutral gas temperature distribution.

$$\nabla \cdot (\rho \mathbf{u}) = 0, \quad (1)$$

$$\rho(\mathbf{u} \cdot \nabla) \mathbf{u} = -\nabla p + \nabla \cdot [\mu(\nabla \mathbf{u} + (\nabla \mathbf{u})^T)] + \mathbf{F}, \quad (2)$$

$$\frac{\partial(\rho \omega_i)}{\partial t} + \nabla \cdot \mathbf{j}_i = \sum_j R_{ij}, \quad (3)$$

$$\rho C_p \left(\frac{\partial T_g}{\partial t} + \mathbf{u} \cdot \nabla T_g \right) = \nabla \cdot (\kappa \nabla T_g) + q, \quad (4)$$

where ρ is the mixture density, \mathbf{u} is the mass-average velocity, μ is the dynamic viscosity, p is the pressure, and \mathbf{F} is the volumetric force vector. Furthermore, ω_i is the mass fraction, and \mathbf{j}_i is the mass flux of species i . R_{ij} is the rate of production (or loss) of species i in reaction j . T_g is the neutral gas temperature, C_p is the gas heat capacity, and κ is the thermal conductivity; q is the volumetric power deposition in the gas by

Table 1. Chemistry used in the simulation. Some reaction rate coefficients are given by an equation of the form $k = AT^B \exp(-C/T)$.

Helium–nitrogen–oxygen chemistry				
Index	Reaction	Coefficient ^a	Activation (eV)	Ref.
Helium chemistry				
R1	$e + \text{He} \rightarrow e + \text{He}$	b	—	Phelps database
R2	$e + \text{He} \rightarrow e + \text{He}^*$	b	19.8	Phelps database
R3	$e + \text{He} \rightarrow 2e + \text{He}^+$	b	24.6	Phelps database
R4	$e + \text{He}^* \rightarrow 2e + \text{He}^+$	b	4.78	Trinity database
R5	$e + \text{He}_2^* \rightarrow 2e + \text{He}_2^+$	$1.268 \times 10^{-18} T_e^{0.71} \exp(-3.4/T_e)$	3.4	[25, 30]
R6	$2\text{He}^* \rightarrow e + \text{He} + \text{He}^+$	4.5e-16	-15	[25, 27, 30]
R7	$2\text{He}^* \rightarrow e + \text{He}_2^+$	2.03e-15	-19.6	[31]
R8	$\text{He}^+ + 2\text{He} \rightarrow \text{He}_2^+ + \text{He}$	1e-43	—	[25, 27, 30, 32]
R9	$\text{He}^* + 2\text{He} \rightarrow \text{He}_2^* + \text{He}$	1.3e-45	—	[25, 27, 30]
R10	$e + \text{He}^* \rightarrow e + \text{He}$	2.9e-15	-19.8	[31]
R11	$2e + \text{He}^+ \rightarrow e + \text{He}^*$	$5.12 \times 10^{-39} T_e^{-4.5}$	-4.78	[33]
R12	$e + \text{He}^+ \rightarrow \text{He}$	2e-18	-24.6	[34]
R13	$e + \text{He}_2^+ \rightarrow \text{He}^* + \text{He}$	$5.386 \times 10^{-13} T_e^{-0.5}$	-0.2	[25, 27, 30]
R14	$e + \text{He}_2^+ \rightarrow 2\text{He}$	9e-15	-20	[31]
Nitrogen chemistry				
R15	$e + \text{N}_2 \rightarrow e + \text{N}_2$	b	—	Phelps database
R16	$e + \text{N}_2 \rightarrow e + \text{N}_2(\text{rot})$	b	0.02	Phelps database
R17	$e + \text{N}_2 \rightarrow e + \text{N}_2(\text{v}1)$	b	0.29	Phelps database
R18	$e + \text{N}_2 \rightarrow e + \text{N}_2(\text{v}1, \text{res})$	b	0.291	Phelps database
R19	$e + \text{N}_2 \rightarrow e + \text{N}_2(\text{v}2)$	b	0.59	Phelps database
R20	$e + \text{N}_2 \rightarrow e + \text{N}_2(\text{v}3)$	b	0.88	Phelps database
R21	$e + \text{N}_2 \rightarrow e + \text{N}_2(\text{v}4)$	b	1.17	Phelps database
R22	$e + \text{N}_2 \rightarrow e + \text{N}_2(\text{v}5)$	b	1.47	Phelps database
R23	$e + \text{N}_2 \rightarrow e + \text{N}_2(\text{v}6)$	b	1.76	Phelps database
R24	$e + \text{N}_2 \rightarrow e + \text{N}_2(\text{v}7)$	b	2.06	Phelps database
R25	$e + \text{N}_2 \rightarrow e + \text{N}_2(\text{v}8)$	b	2.35	Phelps database
R26	$e + \text{N}_2 \rightarrow e + \text{N}_2(A^3\Sigma_u^+ v = 0-4)$	b	6.17	Phelps database
R27	$e + \text{N}_2 \rightarrow e + \text{N}_2(A^3\Sigma_u^+ v = 5-9)$	b	7	Phelps database
R28	$e + \text{N}_2 \rightarrow e + \text{N}_2(B^3\Pi_g)$	b	7.35	Phelps database
R29	$e + \text{N}_2 \rightarrow e + \text{N}_2(W^3\Delta_g^-)$	b	7.36	Phelps database
R30	$e + \text{N}_2 \rightarrow e + \text{N}_2(A^3\Sigma_u^+ v \geq 10)$	b	7.8	Phelps database
R31	$e + \text{N}_2 \rightarrow e + \text{N}_2(B^3\Sigma)$	b	8.16	Phelps database
R32	$e + \text{N}_2 \rightarrow e + \text{N}_2(a^1\Sigma_u^-)$	b	8.4	Phelps database
R33	$e + \text{N}_2 \rightarrow e + \text{N}_2(a^1\Pi)$	b	8.55	Phelps database
R34	$e + \text{N}_2 \rightarrow e + \text{N}_2(w^1\Delta)$	b	8.89	Phelps database
R35	$e + \text{N}_2 \rightarrow e + \text{N}_2(C^3\Pi)$	b	11.03	Phelps database
R36	$e + \text{N}_2 \rightarrow e + \text{N}_2(E^3\Sigma)$	b	11.87	Phelps database
R37	$e + \text{N}_2 \rightarrow e + \text{N}_2(a^1\Sigma)$	b	12.25	Phelps database
R38	$e + \text{N}_2 \rightarrow e + \text{N}_2(\text{sum})$	b	13	Phelps database
R39	$e + \text{N}_2 \rightarrow 2e + \text{N}_2^+$	b	15.6	Phelps database
R40	$e + \text{N}_2 \rightarrow e + 2\text{N}$	$1 \times 10^{-14} T_e^{0.5} \exp(-16/T_e)$	9.8	[35]
R41	$e + \text{N}_2^+ \rightarrow 2\text{N}$	2e-13	-5.8	[31]
R42	$2e + \text{N}_2^+ \rightarrow \text{N}_2 + e$	$5.651 \times 10^{-39} T_e^{-0.8}$	-15.6	[36]
R43	$\text{N}_2(A^3\Sigma) + \text{N}_2 \rightarrow 2\text{N}_2$	2.2e-20	—	[37]
R44	$2\text{N}_2(A^3\Sigma) \rightarrow \text{N}_2(B^3\Pi) + \text{N}_2$	4e-16	—	[37]
R45	$\text{N}_2(A^3\Sigma) + \text{N} \rightarrow \text{N} + \text{N}_2$	5e-17	—	[37]
Oxygen chemistry				
R46	$e + \text{O}_2 \rightarrow e + \text{O}_2$	b	—	Trinity database
R47	$e + \text{O}_2 \rightarrow e + \text{O}_2(\text{v sum})$	b	0.193	Trinity database
R48	$e + \text{O}_2 \rightarrow e + \text{O}_2(a^1\Delta_g)$	b	0.98	Trinity database
R49	$e + \text{O}_2 \rightarrow e + \text{O}_2(b^1\Sigma_u^+)$	b	1.63	Trinity database
R50	$e + \text{O}_2 \rightarrow e + \text{O}_2(\text{exc})$	b	4.5	Trinity database
R51	$e + \text{O}_2 \rightarrow 2e + \text{O}_2^+$	b	12.06	Trinity database
R52	$e + \text{O}_2 \rightarrow \text{O}^- + \text{O}$	b	3.6	Trinity database
R53	$e + \text{O}_2 \rightarrow e + 2\text{O}$	b	5.58	Trinity database

Table 1. (Continued).

Helium–nitrogen–oxygen chemistry				
Index	Reaction	Coefficient ^a	Activation (eV)	Ref.
R54	$e + O_2 \rightarrow e + O + O(^1D)$	b	8.4	Trinity database
R55	$e + O_2 + M \rightarrow O_2^- + M$	$3.6 \times 10^{-43} T_e^{-0.5}$	—	[33]
R56	$e + O_2^+ \rightarrow 2O$	$1.2 \times 10^{-14} T_e^{-0.7}$	-6.48	[33]
R57	$e + O_2^+ \rightarrow O + O(^1D)$	$8.88 \times 10^{-15} T_e^{-0.7}$	-3.66	[33]
R58	$O_2^+ + O^- \rightarrow O + O_2$	$2 \times 10^{-13} (T_g/300)^{-1}$	—	[33]
R59	$O_2^+ + O^- \rightarrow 3O$	1e-13	—	[33]
R60	$O_2^+ + O^- + N_2 \rightarrow O_3 + N_2$	$2.0 \times 10^{-37} (T_g/300)^{-2.5}$	—	[34]
R61	$O_2^+ + O^- + O_2 \rightarrow O_3 + O_2$	$2.0 \times 10^{-37} (T_g/300)^{-2.5}$	—	[34]
R62	$O_2^+ + O^- + M \rightarrow O_2 + O + M$	$2.0 \times 10^{-37} (T_g/300)^{-2.5}$	—	[34]
R63	$O_2^+ + O_2^- \rightarrow 2O_2$	$2 \times 10^{-13} (T_g/300)^{-1}$	—	[33]
R64	$O_2^+ + O_2^- \rightarrow O_2 + 2O$	1e-13	—	[33]
R65	$O_2^+ + O_2^- + M \rightarrow 2O_2 + M$	$2 \times 10^{-37} (T_g/300)^{-2.5}$	—	[34]
R66	$e + O_4^+ \rightarrow 2O_2$	$3.6 \times 10^{-14} T_e^{-0.5}$	-12.06	[38]
R67	$O_4^+ + O^- \rightarrow O_3 + O_2$	4e-13	—	[34]
R68	$O_4^+ + O_2^- \rightarrow 3O_2$	1e-13	—	[38]
R69	$O_4^+ + O_2^- + M \rightarrow 3O_2 + M$	2e-37	—	[38]
R70	$O^- + O_2 \rightarrow e + O_3$	$5.0 \times 10^{-21} (T_g/300)^{-0.5}$	—	[26, 33]
R71	$O_2^- + O \rightarrow e + O_3$	$1.5 \times 10^{-16} (T_g/300)^{-0.5}$	—	[26, 33]
R72	$O_2^+ + O_2 + M \rightarrow O_4^+ + M$	2.4e-42	—	[38]
R73	$O_4^+ + O \rightarrow O_2^+ + O_3$	3.0e-16	—	[34]
R74	$O + O_2 + N_2 \rightarrow O_3 + N_2$	$1.1 \times 10^{-46} \exp(510/T_g)$	—	[34]
R75	$O + O_2 + O_2 \rightarrow O_3 + O_2$	$6 \times 10^{-46} (T_g/300)^{-2.8}$	—	[33]
R76	$O + O_2 + He \rightarrow O_3 + He$	$3.4 \times 10^{-46} (T_g/300)^{-1.2}$	—	[33]
R77	$O_2 + 2O \rightarrow O_3 + O$	$3.4 \times 10^{-46} (T_g/300)^{-1.2}$	—	[33]
R78	$O + O_2 + O_3 \rightarrow 2O_3$	$2.3 \times 10^{-47} \exp(-1057/T_g)$	—	[34]
R79	$O + O_3 \rightarrow 2O_2$	$8 \times 10^{-18} \exp(-2060/T_g)$	—	[33, 39]
Helium–nitrogen–oxygen interactions				
R80	$He^+ + O^- \rightarrow He + O$	$2 \times 10^{-13} (T_g/300)^{-1.0}$	—	[40]
R81	$He^+ + O^- + M \rightarrow He + O + M$	$2 \times 10^{-37} (T_g/300)^{-2.5}$	—	[33]
R82	$He^+ + O_2^- \rightarrow O_2 + He$	$2.0 \times 10^{-13} (T_g/300)^{-1}$	—	[33]
R83	$He_2^+ + O^- \rightarrow 2He + O$	1e-13	—	[41]
R84	$He_2^+ + O^- + M \rightarrow 2He + O + M$	$2 \times 10^{-37} (T_g/300)^{-2.5}$	—	[41]
R85	$He_2^+ + O_2^- \rightarrow 2He + O_2$	1e-13	—	[41]
R86	$N_2^+ + O^- \rightarrow N_2 + O$	$2.0 \times 10^{-13} (T_g/300)^{-0.5}$	—	[42]
R87	$N_2^+ + O_2^- \rightarrow N_2 + O_2$	$2.0 \times 10^{-13} (T_g/300)^{-0.5}$	—	[42]
R88	$He^+ + N_2 \rightarrow N_2^+ + He$	5e-16	—	[36]
R89	$He_2^+ + N_2 \rightarrow N_2^+ + 2He$	5e-16	—	[36]
R90	$He_2^+ + N_2 \rightarrow N_2^+ + He_2^*$	1.4e-15	—	[43]
R91	$O^- + N_2(A^3\Sigma) \rightarrow N_2 + O + e$	2.2e-15	—	[37]
R92	$O_2^- + N_2(A^3\Sigma) \rightarrow N_2 + O_2 + e$	2.1e-15	—	[37]
R93	$N_2(A^3\Sigma) + O_2 \rightarrow N_2 + 2O$	$5 \times 10^{-18} \exp(-200/T_g)$	—	[37]
R94	$N_2(A^3\Sigma) + O_2 \rightarrow O_2(a^1\Delta_g) + N_2$	1e-18	—	[37]
R95	$He^* + O_3 \rightarrow O_2^+ + O + He + e$	$2.54 \times 10^{-24} (T_g/300)^{-0.5}$	-2.15	[26, 33]
R96	$N + O + M \rightarrow NO + M$	$5.5 \times 10^{-45} \exp(155/T_g)$	—	[44]
R97	$N_2(A^3\Sigma) + O \rightarrow NO + N$	7e-18	—	[42]
R98	$He^* + N_2 \rightarrow e + N_2^+ + He$	5e-17	-4.2	[43]
R99	$He_2^* + N_2 \rightarrow e + N_2^+ + 2He$	3e-17	-1	[43]
R100	$He^* + O_2 \rightarrow e + O_2^+ + He$	2.6e-16	-7.74	[30]
R101	$He_2^* + O_2 \rightarrow e + O_2^+ + 2He$	3.6e-16	-4.54	[30]

^a Rate coefficient in m^3s^{-1} for 2-body reactions, and m^6s^{-1} for 3-body reactions. T_e in eV and T_g in K.^b Rate coefficients calculated using cross-section data from the indicated reference. Species M in reactions represents a third-body.

the plasma. The mass flux included contributions by ordinary diffusion (first term on the right hand side of equation (5)) and bulk flow.

$$j_i = -\rho D_i^m \nabla \omega_i + \rho \omega_i u. \quad (5)$$

Here, $D_i^m = \frac{1-\omega_i}{\sum_{k \neq i} \frac{x_k}{D_{ik}}}$ is the mixture-averaged diffusion coefficient of species i , where D_{ik} is the binary diffusion coefficient between species i and k , calculated using the Chapman–Enskog theory [45]; x_k is the mole fraction of species k . Note that the neutral gas convective mass and heat transport model is applied at steady-state without chemical reactions. Therefore, in equations (3) and (4), the time dependent and reaction terms were set equal to zero. The boundary conditions for this model corresponded to those in [25]. The pure helium gas velocity was specified at the inlet of the central tube (in plug flow), and the pure nitrogen shielding gas velocity was specified at the inlet of the annular space formed by the coaxial tubes (figure 1), also in plug flow. The total pressure was specified (1 atm) at the exit. The gas velocity was set equal to zero on walls (no slip condition). Walls were considered to be impermeable to gases. There was no change in species density at the exit. The ambient air mass flow rate at the domain boundaries LM and MN shown in figure 1 (middle panel) was set proportional to that of the shielding gas mass flow rate $Q_{\text{air}} = 0.03 Q_{\text{N}_2}$ [46].

2.2. Plasma dynamics model

The 2-D plasma dynamics model used the fluid approach, based on the species continuity equations (equation (6)), with the drift-diffusion approximation (equation (7)), the electron energy conservation equation (equation (8)), and Poisson's equation (equation (9)) for the electrostatic field

$$\frac{\partial n_i}{\partial t} + \nabla \cdot \Gamma_i = \sum_j R_{ij}, \quad (6)$$

$$\Gamma_i = Z_i n_i \mu_i E - D_i \nabla n_i + u n_i, \quad (7)$$

$$\begin{aligned} \frac{\partial (n_\epsilon)}{\partial t} + \nabla \cdot \left(-\frac{5}{3} \mu_e E n_\epsilon - \frac{5}{3} D_e \nabla n_\epsilon \right) = -\Gamma_e \cdot E \\ - \sum_j \Delta E_j R_{\text{inel},j} - 3 \frac{m_e}{M} k_b n_e \nu_{\text{en}} (T_e - T_g), \end{aligned} \quad (8)$$

$$\epsilon_0 \nabla \cdot (\epsilon_r \nabla \Phi) = - \sum_i Z_i n_i, \quad (9)$$

where n_i is the number density of species i , R_{ij} is the rate of production or loss of species i in reaction j , Γ_i is the total flux of species i in the drift-diffusion approximation, is electric field, μ_i is mobility, D_i is diffusivity and Z_i is the charge number of species i (zero for neutral species). Electron mobility was found by solving the Boltzmann equation (BOLSIG+[47]) in the two-term approximation. The electron diffusivity was calculated using the Einstein relation $D_e = \mu_e k_b T_e$, where k_b

is the Boltzmann constant, and T_e is electron temperature, assuming a Maxwellian electron energy distribution function. The ion diffusivity D_{ion} was estimated by the Chapman–Enskog theory, and the ion mobility, μ_{ion} , was obtained from the Einstein relation $D_{\text{ion}} = \mu_{\text{ion}} k_b T_g$, where T_g is the gas temperature.

In the electron energy conservation equation (8) $n_\epsilon = \frac{3}{2} n_e T_e$ is electron energy density. ΔE_j and $R_{\text{inel},j}$ are electron energy loss (or gain) due to inelastic collision, j , and the corresponding reaction rate, respectively. The right-hand side of the electron energy equation (8) includes Joule heating, inelastic collisional energy exchange, and energy exchange of electrons suffering elastic collisions with neutrals, where m_e is electron mass, M is heavy species mass, and ν_{en} is the electron-neutral elastic collision frequency. In Poisson's equation (9), Φ is the electrostatic potential, ϵ_0 is vacuum permittivity, and ϵ_r is relative permittivity (unity for the gas phase and 4.5 for quartz).

The boundary conditions for the plasma dynamics model were similar to the corresponding boundary conditions in ref [25]. The normal flux of particles (electrons, ions, metastables) and the electron energy flux on walls were described by equations (10)–(13) below. The potential on dielectrics surfaces was found using Gauss' law, as in [25].

$$\Gamma_e \cdot n = \frac{1}{4} n_e \sqrt{\frac{8k_b T_e}{\pi m_e}} - \alpha_s \sum_i \gamma_i (\Gamma_i \cdot n) + \alpha'_s \mu_e n_e E, \quad (10)$$

$$\Gamma_i \cdot n = \frac{1}{4} n_i \sqrt{\frac{8k_b T_i}{\pi m_i}} + \alpha'_s \mu_i n_i E, \quad (11)$$

$$\Gamma_m \cdot n = \frac{2\gamma_m}{2-\gamma_m} \frac{1}{4} n_m \sqrt{\frac{8k_b T_g}{\pi m_m}}, \quad (12)$$

$$\Gamma_\epsilon \cdot n = \frac{1}{2} n_\epsilon \sqrt{\frac{8k_b T_e}{\pi m_e}} - \alpha_s 2k_b T_e \sum_i \gamma_i (\Gamma_i \cdot n), \quad (13)$$

where γ_m is the probability of deactivation of metastables in collisions with a wall (assumed unity), and α_s and α'_s are switching functions depending on the sign of the dot product of E and n [25], where n is the unit vector normal to the surface, pointing towards the surface.

2.3. Method of solution

The two equation systems were solved sequentially, in a time-implicit manner, using the finite element method, implemented in COMSOL [48]. The neutral gas convective mass and heat transport equations (1)–(4) were solved first, using a standard non-linear solver based on a quasi-Newton iteration scheme, to obtain the steady-state profiles of gas velocity, temperature, and mass (mole) fractions of helium, nitrogen, oxygen and argon. In turn, these profiles were used as inputs to the plasma dynamics model. Equations (6)–(9) were solved using PARDISO, a time-dependent

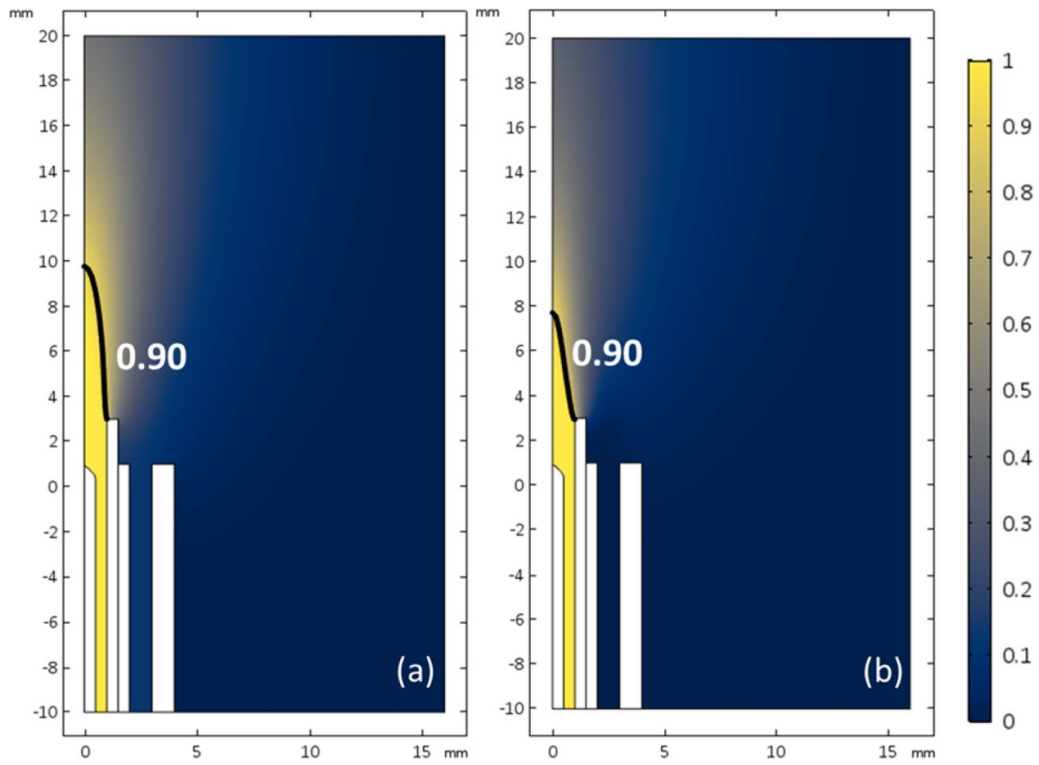


Figure 2. Helium mole fraction distribution without shielding gas (a), and with shielding gas (b). The vertical axis indicates axial position in mm. The tip of the needle is at 1 mm. The horizontal axis is radial position in mm.

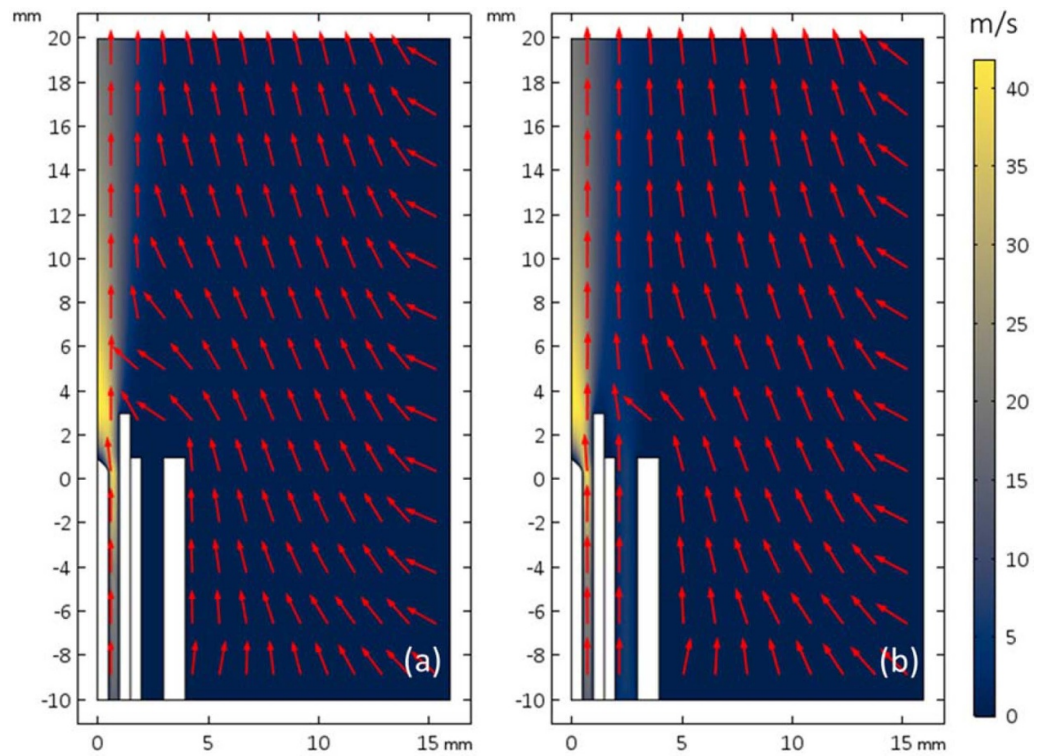


Figure 3. Profiles of the magnitude of gas velocity (color scale bar) without shielding gas (a), and with shielding gas (b). Arrows show the velocity direction (not the magnitude). The vertical axis indicates axial position in mm. The tip of the needle is at 1 mm. The horizontal axis is radial position in mm.

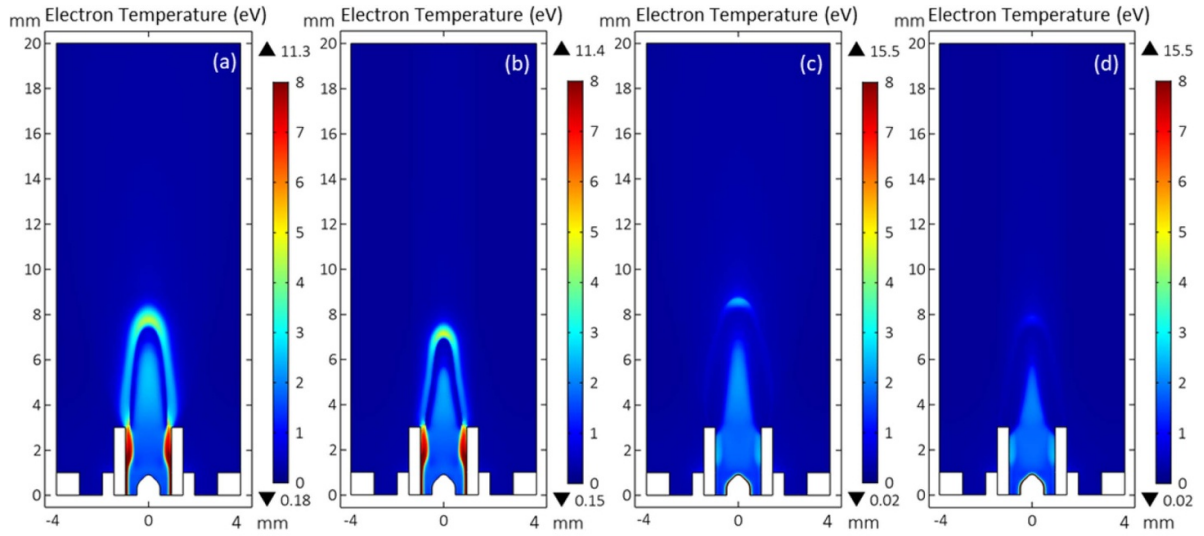


Figure 4. Electron temperature (eV) distribution at positive peak voltage (a) (b), and negative peak voltage (c) (d), of the applied RF waveform, without shielding gas (a) (c), and with shielding gas (b) (d). The vertical axis indicates axial position in mm. The tip of the needle is at 1 mm. The horizontal axis is radial position in mm.

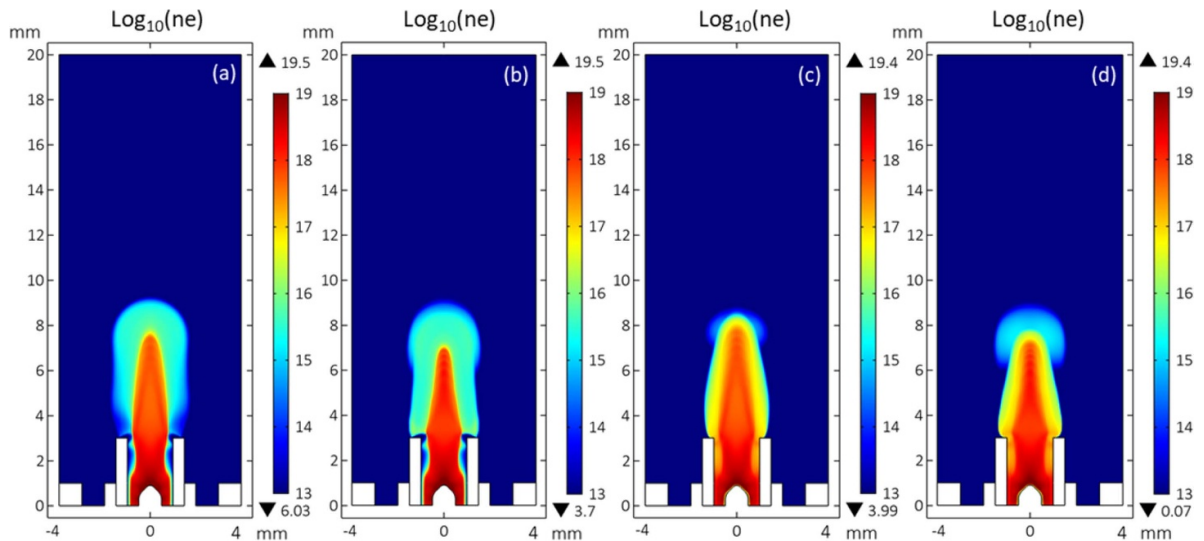


Figure 5. Electron density (\log_{10} scale, 1 m^{-3}) distribution at positive peak voltage (a) (b), and negative peak voltage (c) (d), of the applied RF waveform, without shielding gas (a) (c), and with shielding gas (b) (d). The vertical axis indicates axial position in mm. The tip of the needle is at 1 mm. The horizontal axis is radial position in mm.

solver, for tens of radio-frequency (RF) cycles, to obtain electron density and electron temperature profiles as well as the plasma species concentration profiles. Since the timescale of the neutral gas (ms) is much longer than that of plasma dynamics (ns), this method of separation of the neutral and plasma flows is valid. A similar approach was followed by Breden and Raja [26]. In the present work, the minimum finite element size of $1 \mu\text{m}$ was employed near the needle electrode. A typical simulation involved about a million degrees of freedom. In the next section, simulation predictions of APPJ characteristics with and without shielding gas are reported and compared, side-by-side. Comparison with experimental data obtained in our laboratory is also presented and discussed.

3. Results and discussion

3.1. Properties of the neutral gas

Figure 2 shows the two-dimensional helium mole fraction distribution, with and without shielding gas, for the base case conditions (He flow of 2 slm, N_2 flow of 4.5 slm). Outlines of the needle powered electrode, central tube, outer tube and grounded electrode are also shown. Inside the central tube, the mole fraction of helium is almost unity, since the Peclet number ($Pe = uL/D$; u is average flow velocity, D is diffusivity and L is characteristic length) $Pe \sim 2000$ of the working gas is high enough to prevent back diffusion of the shielding or ambient gases into the central tube. Outside the central tube,

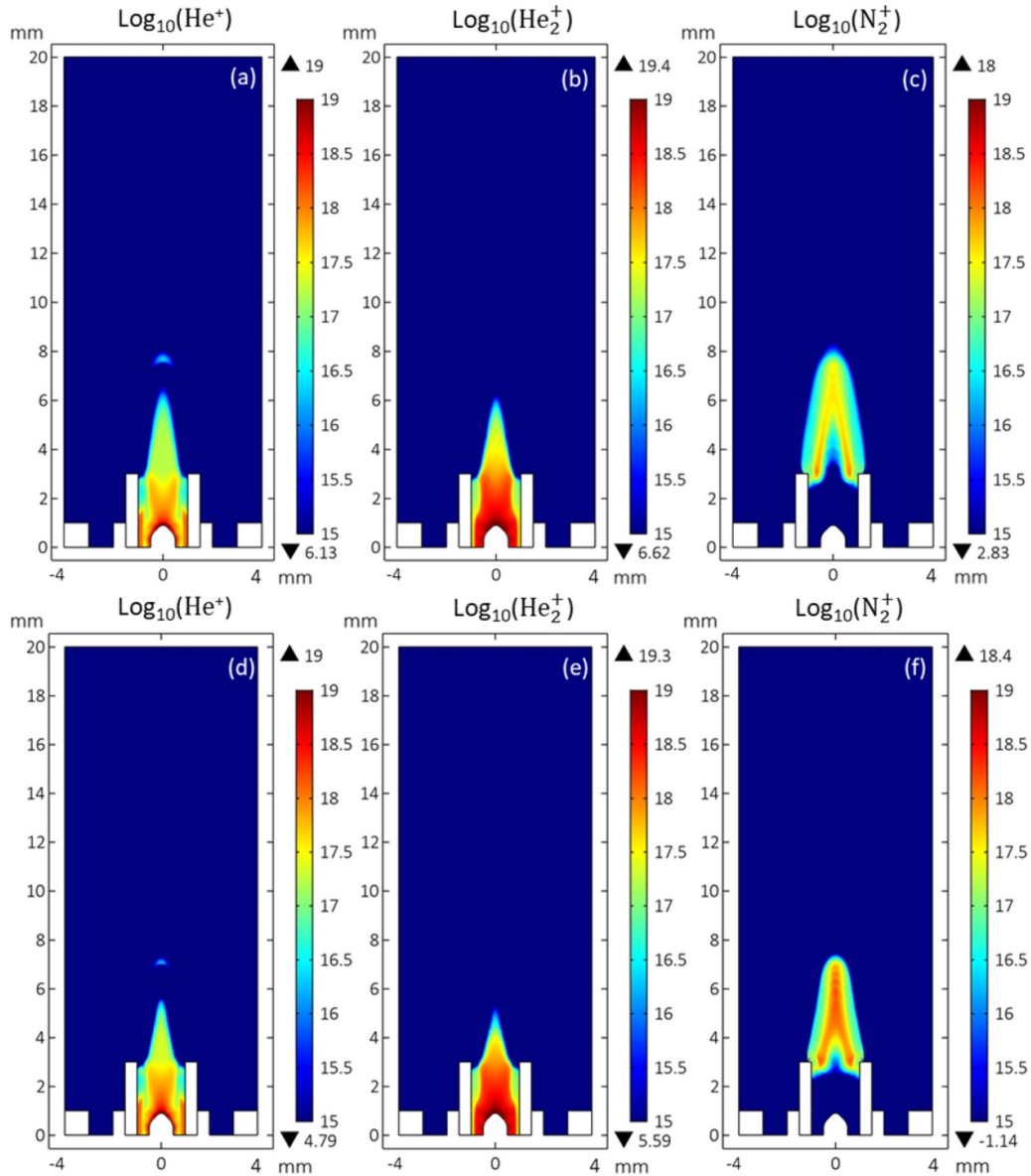


Figure 6. Spatial distribution of the density ($\log_{10}, 1 \text{ m}^{-3}$) of He^+ , He_2^+ and N_2^+ without shielding gas (a), (b), (c), and with shielding gas (d), (e), and (f). The vertical axis indicates axial position in mm. The tip of the needle is at 1 mm. The horizontal axis is radial position in mm.

shielding gas and ambient gas components diffuse into the helium column, causing the helium mole fraction to decrease gradually with axial distance from the nozzle and radial distance from the centerline. The locus of points where the He mole fraction is 0.9 is shown as a black line superimposed on the mole fraction distribution. Without shielding gas, the intersection of the 0.9 helium mole fraction contour with the system axis occurs about 7 mm from the nozzle (the nozzle is at axial distance $z = 3$ mm), compared to about 5 mm from the nozzle in the case with nitrogen shielding gas. This implies that more nitrogen invades the helium core for the case of shielding gas. This is because the shielding gas is 100% nitrogen, as opposed to 78% nitrogen without shielding gas, and also, the shear at the interface between the central and annular jets enhances the rate of mass transport.

Comparisons using different He mole fraction contours led to the same conclusions. The helium mole fraction in the jet is important for guiding the plasma plume. In fact, the plasma plume was predicted to extend a longer distance from the nozzle in the case without shielding gas (see below), and this was verified by visual observations in our laboratory APPJ reactor.

The magnitude (color scale bar) and direction (arrows) of the gas velocity, for the base case conditions, are displayed in figure 3. The red arrows show the direction of velocity (not the magnitude). In the jet region, the velocity is highest in the domain $r < 1$ mm where the core of the central jet is located. The flow first accelerates as the entering helium gas is heated by the needle. (due to the high thermal conductivity of the metal, the temperature of the needle is uniform at 500 K.) Then

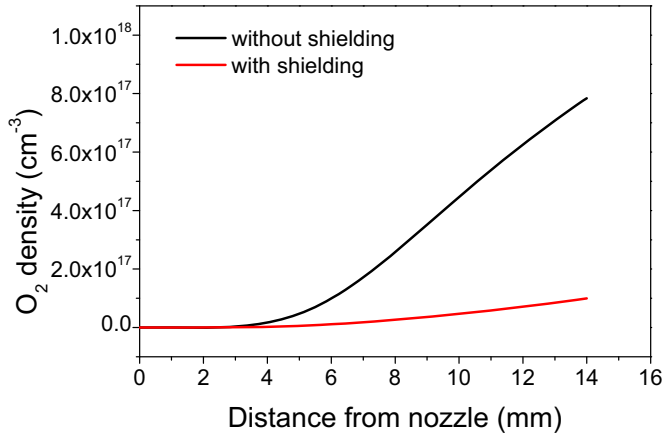


Figure 7. On-axis O₂ number density as a function of distance from the nozzle with and without shielding gas.

the helium velocity decreases, over a short axial distance, once the flow has cleared the needle tip, and the cross sectional area available for flow increases. (in fact there is a flow recirculation zone over the needle tip that cannot be resolved in the scale of the figure). The gas accelerates again as it enters the region of highest gas temperature near the nozzle (see section 3.3 below). The flow velocity goes through a maximum near the nozzle, and decreases downstream as the jet is expanding and the gas cools down. The shielding gas flow is almost parallel to the helium core flow and sweeps the entrained ambient gases downstream.

3.2. Plasma properties

In figure 4, the electron temperature distributions are displayed at two phase angles of the applied RF voltage (at peak positive and peak negative voltage) with and without shielding gas. The maximum electron temperature at a given phase does not depend on the presence or absence of shielding gas since the maximum occurs inside the central tube. The same holds true for the electron density, shown in figure 5. The peak electron density is of the order of 10^{19} m^{-3} . The head of the plasma plume is closer to the nozzle with shielding gas compared to without shielding gas. This implies a shorter plasma plume consistent with the 0.9 helium mole fraction contour being closer to the nozzle, in the case with shielding gas (figure 2). Furthermore, the electron temperature at the positive peak voltage is higher compared to the negative peak voltage. The maximum T_e at positive peak voltage is near the dielectric tube while the maximum T_e at negative peak voltage is near the needle tip (figure 4). Outside the tube, there are two relatively high electron temperature regions, one in the mixing layer and another in the head of the streamer, where the electric field is high.

The electron density is radially confined by a self-developed radial electric field that prevents further out-diffusion of electrons. Also, the electron density profile does not change significantly when the phase of the RF cycle swings from peak positive to peak negative voltage. At 13.7 MHz, used in this work, helium ions have only a sluggish response

to the variations of the field, i.e. the ion density in the bulk is hardly modulated. Since the electron density in the bulk is equal to the ion density to satisfy electro-neutrality electrons are also hardly modulated in the RF cycle.

Figure 6 shows ion density profiles with and without shielding gas. Inside the tube, He_2^+ and He^+ are dominant ions due to the gas being pure helium inside. In the mixing layer He_2^+ is consumed by charge exchange with N_2 (R89 and R90, table 1). He^+ is produced mainly by electron impact ionization of ground-state He atoms (R3). He^+ is converted to He_2^+ by three-body reaction (R8). The density of He^+ follows a similar spatial profile as that of He_2^+ inside the tube. Outside the tube, the He^+ profile is different from that of He_2^+ . The He^+ number density outside the tube is lowered since He^+ is lost by charge exchange with N_2 (R88) in the mixing layer, and by reaction (R8) to produce He_2^+ in the center of the plasma jet. At $z = 8 \text{ mm}$ on-axis, the He^+ number density is about $3.2 \times 10^{16} \text{ m}^{-3}$, but at the same position the He_2^+ number density is smaller. With shielding gas, the plume of helium ions outside the tube is shorter compared to without shielding gas as explained before. The presence of shielding gas has a minor effect on the density profiles of the helium ions since these profiles develop upstream of the nozzle and are little influenced by the gases outside the tube. The N_2^+ mainly occurs in the mixing layer outside the tube. The N_2^+ number density profile near the nozzle is donut-shaped, but the donut hole shrinks with increasing distance from the nozzle, only to disappear at a distance of about 5.5 mm. With shielding gas, the N_2^+ number density is much higher in the mixing layer than the case without shielding gas.

In figure 7, the on-axis O₂ number density increases with distance from the nozzle, both with and without shielding gas. The O₂ density is lower in the presence of shielding gas, and is vanishingly small up to a distance of 3 mm downstream of the nozzle. Indeed, in the first few mm downstream of the nozzle, the O₂ density is determined by the oxygen impurity in the helium gas feed. With increasing distance from the nozzle, there is widening of the difference of O₂ number density without shielding gas compared to that with shielding gas. In any case, the O₂ density with shielding gas is several times lower than without shielding gas. Very similar behavior to that shown in figure 7 has been reported by Reuter *et al* [8].

3.3. Gas temperature distribution

To facilitate the imposition of boundary conditions on the equation of convective heat transport (equation (4)), both the inner and outer tube as well as the needle, were extended 10 mm upstream of the nozzle as shown in figure 1 (middle panel), so that the feed gases could be assumed to enter at 300 K at the extended inlets. The needle was assumed isothermal due to the high thermal conductivity of the metal. The needle temperature was taken to be 500 K, as measured experimentally with a thermocouple. The power deposited by the plasma into the gas was taken to be 16.5 W, found by matching the temperatures predicted by the simulation with the measured gas temperatures, 5 mm from the nozzle and at radial position of 1 mm, with shielding gas (825 K) and without shielding gas (1000 K, figure 8).

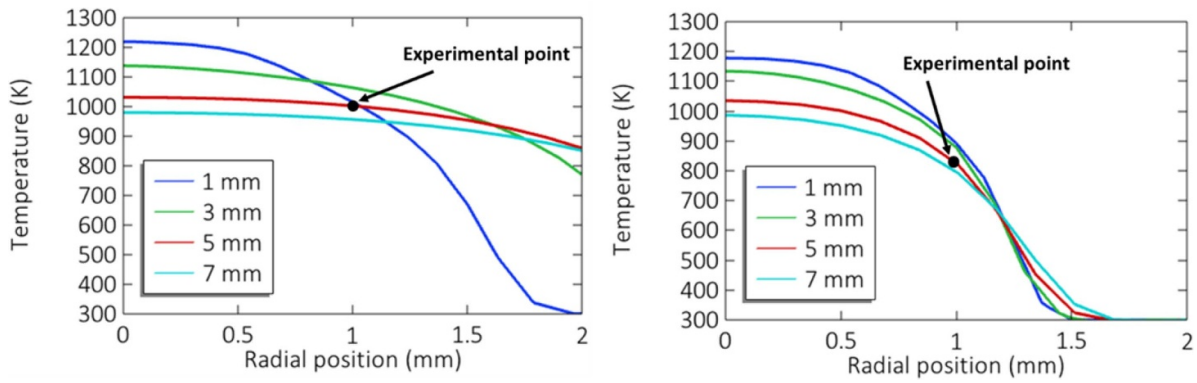


Figure 8. Predicted radial distribution of gas temperature at several distances from the nozzle, without shielding gas (left) and with shielding gas (right). The model predictions of gas temperature were matched to the experimentally obtained temperatures at two points (5 mm from nozzle at a radial position of 1 mm) as shown. Base case conditions.

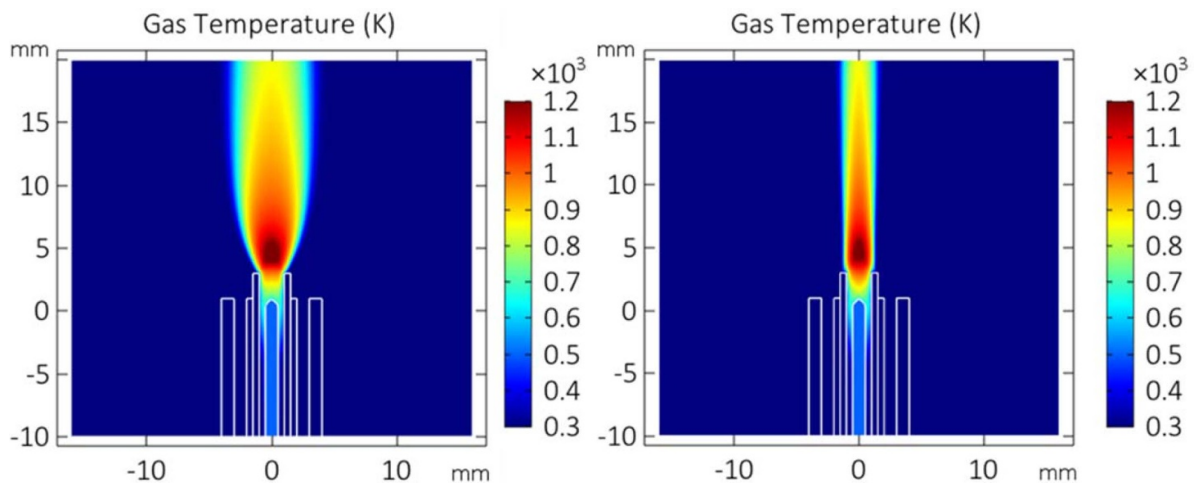


Figure 9. Gas temperature distribution without shielding gas (left) and with shielding gas (right), for the base case conditions. The vertical axis indicates axial position in mm. The tip of the needle is at 1 mm. The horizontal axis is radial position in mm.

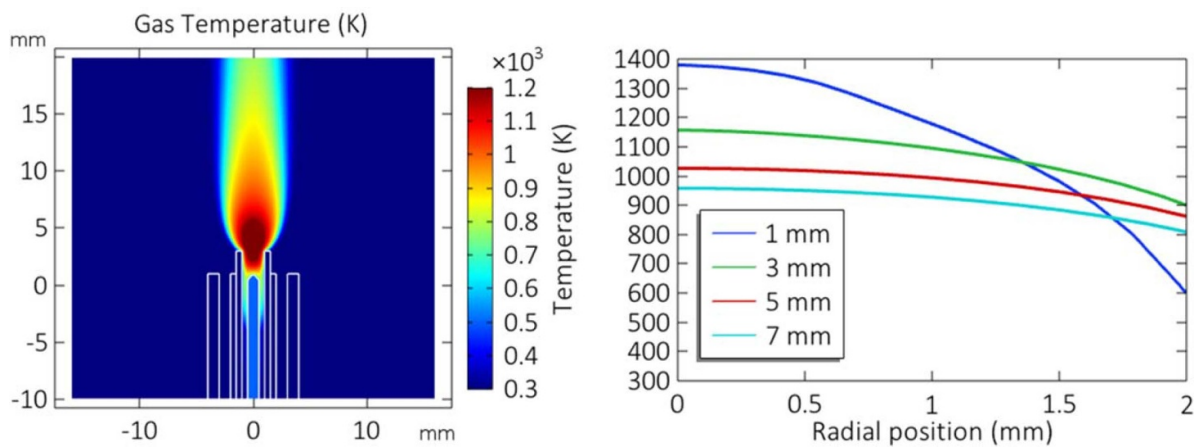


Figure 10. Gas temperature distribution for a helium flow rate of 1 slm without shielding gas. For the left panel, the vertical axis indicates axial position in mm. The tip of the needle is at 1 mm. The horizontal axis is radial position in mm.

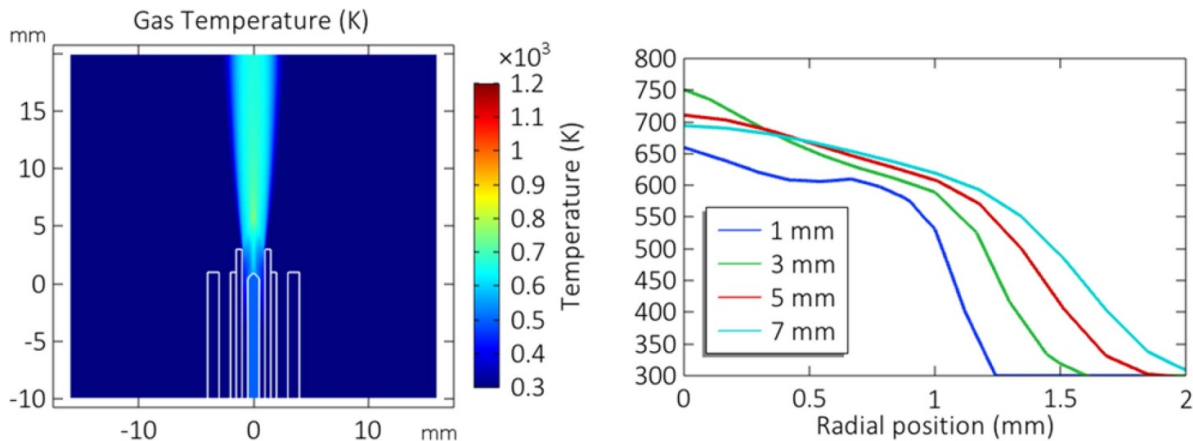


Figure 11. Gas temperature distribution for a helium flow rate of 5 slm, without shielding gas. For the left panel, the vertical axis indicates axial position in mm. The tip of the needle is at 1 mm. The horizontal axis is radial position in mm.

Figure 9 shows the gas temperature distribution with and without shielding gas, for the base case conditions. Without shielding gas, the temperature peaks on-axis, and has a maximum value of 1220 K, at an axial distance of 1 mm from the nozzle. In general, the temperature decreases both axially and radially. The radial profile becomes more uniform with increasing distance downstream aided by the high thermal conductivity of helium. With shielding gas, the temperature also peaks on axis but the radial extent of the high temperature zone shrinks due to the cooling effect of the shielding gas. Figure 8 shows that the temperature profiles within a radial distance of about 0.8 mm are similar with or without shielding gas. Beyond 0.8 mm, the temperature profiles with shielding gas vary over a much tighter range and sustain much sharper gradients, again due to the cooling effect of the shielding gas.

For a helium flow rate of 1 slm (figure 10), the high-temperature zone is partly inside the central tube and the maximum temperature is about 1380 K at the distance 1 mm from the nozzle. With 2 slm helium flow (figure 9), the maximum temperature decreases to about 1220 K. By increasing the helium flow rate to 5 slm, the gas temperature decreases drastically, especially inside the tube; and the high-temperature zone becomes very slim. The decrease of maximum temperature with increasing flow rate is due to convective cooling of the gas (heat removal by the flow). Figure 11 shows that the on-axis temperature ranges from 660 K at an axial distance of 1 mm from the nozzle to 750 K at an axial distance of 3 mm from the nozzle. Interestingly, in this case, the on-axis temperature increases over a range of axial distances from the nozzle, due to the highly convective nature of the flow. The significant effect of flow on gas temperature in an atmospheric pressure microplasma was discussed by Wang *et al* [49].

Figure 12 shows the predicted radial profiles of the mole fractions of N_2 , O_2 and Ar at three axial positions in the jet (1 mm, 3 mm, and 5 mm from the nozzle). The case of no shielding gas (left column panels a, b, c) is compared to that

with shielding gas (right column, panels d, e, f). The mole fractions of O_2 and Ar are quite low, especially in the presence of the shielding gas, and close to the nozzle where the convective flow of the working gas does not allow any back diffusion of gases. For all three axial locations, the N_2 mole fraction increases, while the mole fractions of O_2 and Ar both decrease with the nitrogen shielding gas on. At axial position of 3 mm from the nozzle, the on-axis O_2 and Ar mole fractions decrease from 3.9×10^{-4} to 6.8×10^{-5} and from 1.9×10^{-5} to 3.3×10^{-6} , respectively, in the presence of shielding gas. The radial profiles dip on axis and increase monotonically as a function of radius, more so closer to the nozzle. The radial gradients are severe at 1 mm from the nozzle (note log scale), but the profiles tend to flatten out with increasing distance from the nozzle, as the exposure time increases. The Ar mole fraction at 1 mm from the nozzle is less than 10^{-7} for radii smaller than 0.2 mm (figure 12(d)). The mole fractions of argon and molecular oxygen are so low near the nozzle (especially with the shielding gas on) that the mole fraction of these gases in practical systems may be determined by impurities in the He feed gas. A rather comprehensive comparison between simulation predictions with experimental measurements of species (O_2 , N_2 and Ar) mole fraction radial profiles, at several axial distances from the nozzle, with and without shielding gas, is presented in [50].

3.4. Comparison with experimental data

An APPJ reactor in our laboratory was employed to test simulation predictions against experimental measurements, under identical geometric and operating conditions. The species mole fraction was measured using optical emission spectroscopy combined with a technique called self-actinometry [50]. Figure 13 shows the on-axis mole fraction of O_2 , N_2 and Ar at three distinct axial distances from the nozzle. The nitrogen mole fraction 1 mm from the nozzle was exceedingly low, so the corresponding experimental point is missing. For all

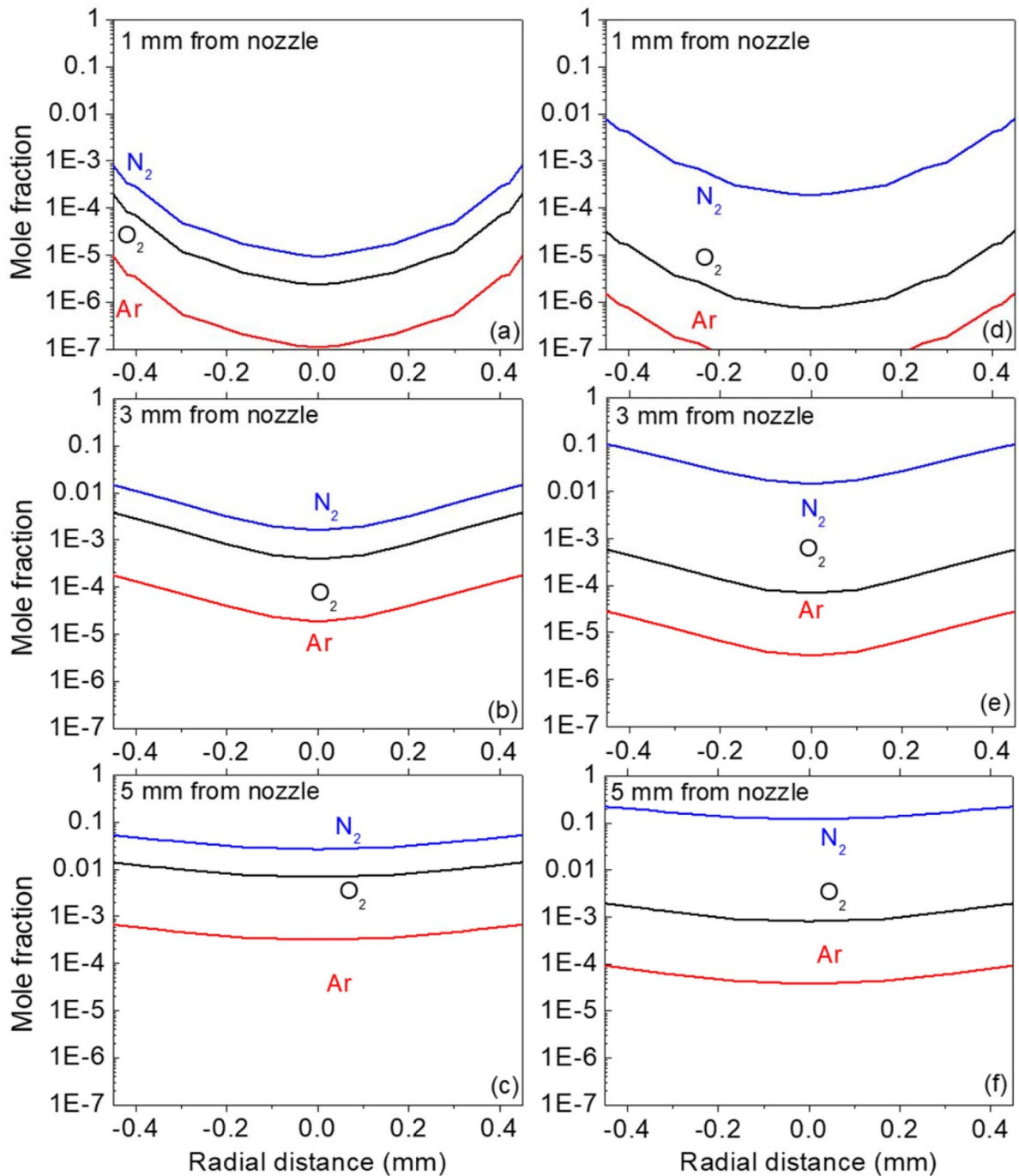


Figure 12. Predicted radial profiles of the mole fraction of N_2 , O_2 and Ar at three axial positions in the jet (1 mm, 3 mm, and 5 mm from the nozzle). The case of no shielding gas (left column a, b, c) is compared to that with shielding gas (right column, d, e, f).

three species, the simulation results are in reasonable agreement with the experimental data at 3 mm distance from the nozzle. At 1 mm from the nozzle, the Ar mole fraction is predicted to be several times lower than the experimental value, because at this location the minority species mole fraction is determined by the impurities of the helium feed gas, and such impurities were not included in the simulation. At 3 mm and 5 mm from the nozzle, the air species have diffused enough into the jet to overpower the density of impurities. At 5 mm, the agreement is reasonable, except for O_2 , whose mole fraction

is predicted to be several times higher than the experimental value. In addition, for all three species, the mole fraction ratio between 3 mm and 1 mm from the nozzle is much higher than the ratio between 5 mm and 3 mm from the nozzle. Overall, the simulation captures the salient features of the experimental measurements.

In figure 14, the measured intensity of the helium excited state ($He\ 3^3S$), emitting at 706 nm, is found by Abel inverted line-integrated experimental data and compared with simulation predictions as a function of radius. Quenching of the

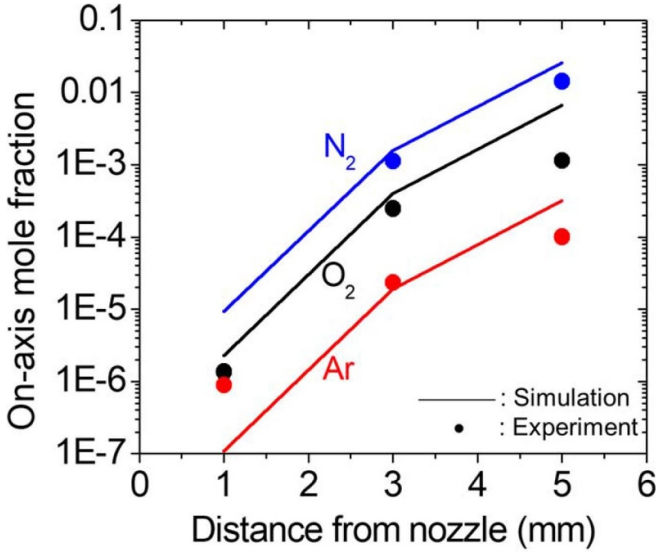


Figure 13. Comparison between simulation predictions with experimental data (points) of the on-axis mole fraction of O₂, N₂ and Ar without shielding gas. The simulation values at the three axial locations are shown connected with straight lines.

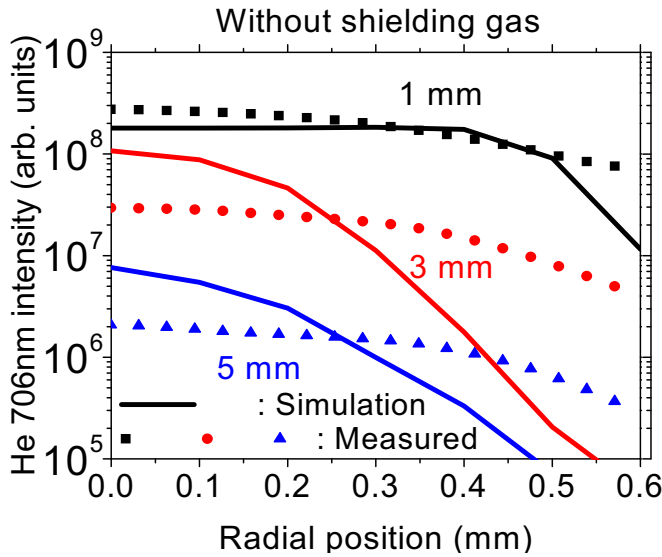


Figure 14. Radial distribution of light intensity of He excited state (emitting at 706 nm) under base case conditions, for three axial distances from the nozzle. Simulation predictions (lines) are compared to experimental data (points).

excited state in collisions with oxygen and nitrogen was taken into account. The rate coefficient for quenching by nitrogen at 600 K is $5 \times 10^{-10} \text{ cm}^3 \text{ s}^{-1}$ [51, 52]. The inverse of the natural lifetime [53] of the excited state $1/\tau_0$ is $2.63 \times 10^7 \text{ s}^{-1}$. The rate coefficient for quenching by oxygen was assumed to be the same as that by nitrogen. The equations used to calculate

the emission intensity were,

$$K(T_e) = \sqrt{\frac{2}{m_e}} \int_0^\infty \sigma(\varepsilon) f(\varepsilon) \varepsilon d\varepsilon, f(\varepsilon) = \frac{2}{\sqrt{\pi}} \frac{\exp\left(-\frac{\varepsilon}{kT_e}\right)}{(kT_e)^{3/2}} \quad (14)$$

$$k_q(T_g) = k_q(T_r) \sqrt{\frac{T_g}{T_r}} \quad (15)$$

$$R = Kn_e n_{\text{He}} \quad (16)$$

$$I \sim \frac{\tau_0^{-1}}{\tau^{-1}} R \quad (17)$$

$$\tau^{-1} = \tau_0^{-1} + k_{qN_2} n_{N_2} + k_{qO_2} n_{O_2} \quad [52] \quad (18)$$

where $K(T_e)$ is the excitation rate coefficient (a function of electron temperature), and ε is the electron energy. A Maxwellian EEDF is assumed in equation (14); T_r is a reference temperature for quenching rate coefficient k_q , R is the electron impact excitation rate to the He 3^3S state, I is the calculated emission intensity; τ and τ_0 are species effective lifetime and natural lifetime, respectively. Finally, k_{qN_2} and k_{qO_2} are the quenching rate coefficients for N₂ and O₂, respectively. The emission intensity was calculated from equation (17) using the electron density and temperature as well as the densities of N₂ and O₂ found by the simulation.

Figure 14 shows that, in both simulation and experiments, the emission intensity peaks on axis and decreases monotonically along the radius of the plasma jet. Also, the on-axis intensity decreases by more than an order of magnitude in going from 1 mm to 3 mm from the nozzle. As seen in figures 4 and 5, the on-axis electron density and temperature do not change significantly in going from axial position $z = 4 \text{ mm}$ (1 mm from the nozzle) to $z = 6 \text{ mm}$ (3 mm from the nozzle). Thus, the dramatic fall in emission intensity between 1 mm and 3 mm from the nozzle must be attributed to quenching of the excited state as the oxygen and nitrogen mole fractions increase drastically from 1 mm to 3 mm (figure 12). The simulated intensity falls off faster than the measurements at large radii. This may be due to overestimation of the quenching of the excited state by nitrogen and oxygen. Nevertheless, the main features of the experimental data are again captured by the simulation.

4. Summary and conclusions

A two-dimensional (r ; z) numerical simulation of a non-equilibrium APPJ in helium, with co-axial nitrogen shielding gas was performed. The shielding gas provided a curtain hindering penetration of the ambient gas (here dry air 78%N₂-21%O₂-1%Ar) into the helium jet. A neutral gas convective

mass and heat transport model was combined with a fluid plasma dynamics model to predict the APPJ discharge characteristics. Results for an APPJ with nitrogen shielding gas were compared to an otherwise identical APPJ without shielding gas. Furthermore, simulation predictions of ambient species mole fractions in the jet, and optical emission intensity profiles of the He 3^3S excited state, were compared to experimental measurements in an APPJ in our laboratory.

The presence of nitrogen shielding gas resulted in a concentration of ambient species (oxygen and argon) in the core of the jet several times lower compared to the case of no shielding gas. For the base case (He flow of 2 slm), switching on the N_2 shielding gas flow (at 4.5 slm) reduced the on-axis O_2 and Ar mole fractions from 3.9×10^{-4} to 6.8×10^{-5} and from 1.9×10^{-5} to 3.3×10^{-6} , respectively, at an axial distance of 3 mm from the nozzle. In addition, in the presence of shielding gas, N_2 penetrated deeper into the helium jet, leading to a shorter plasma plume beyond the nozzle, in agreement with experimental observations. The ambient species mole fraction radial profiles were center-low for short axial distances from the nozzle (~ 1 mm), but became progressively flatter at longer distances from the nozzle. Increasing the He working gas flow rate resulted in lower gas temperature. The maximum temperature occurred a small distance from the nozzle (depending on flow rate) and decreased from ~ 1400 K for 1 slm, to ~ 1200 K for 2 slm, to ~ 800 K for 5 slm of He flow through the central tube of the co-axial configuration. In the presence of shielding gas, the radial extent of the high gas temperature zone was significantly reduced, but the maximum temperature was mostly unaffected. Simulation predictions captured the salient features of experimental measurements of ambient species mole fraction in the jet, and optical emission (706 nm) intensity profiles of the He 3^3S excited state.

Acknowledgments

The authors are grateful to the Department of Energy, Office of Fusion Energy Science, contract No. DE-SC0001939 for financial support of this work.

ORCID iDs

Peng Lin  <https://orcid.org/0000-0001-7703-7838>
 Jiao Zhang  <https://orcid.org/0000-0002-2761-792X>
 Tam Nguyen  <https://orcid.org/0000-0002-9240-1615>
 Vincent M Donnelly  <https://orcid.org/0000-0001-5834-6678>
 Demetre J Economou  <https://orcid.org/0000-0001-6272-4862>

References

- [1] Graves D B 2014 Low temperature plasma biomedicine: a tutorial review *Phys. Plasmas* **21** 080901
- [2] Weltmann K D and Von Woedtke Th 2017 Plasma medicine—current state of research and medical application *Plasma Phys. Control. Fusion* **59** 014031
- [3] Laroussi M, Lu X and Keidar M 2017 Perspective: The physics, diagnostics, and applications of atmospheric pressure low temperature plasma sources used in plasma medicine *J. Appl. Phys.* **122** 020901
- [4] Penkov O V, Khadem M, Lim W S and Kim D E 2015 A review of recent applications of atmospheric pressure plasma jets for materials processing *J. Coatings Technol. Res.* **12** 225–35
- [5] Jiang B, Zheng J, Qiu S, Wu M, Zhang Q, Yan Z and Xue Q 2014 Review on electrical discharge plasma technology for wastewater remediation *Chem. Eng. J.* **236** 348–68
- [6] Yue Y, Wu F, Cheng H, Xian Y, Liu D, Lu X and Pei X 2017 A donut-shape distribution of OH radicals in atmospheric pressure plasma jets *J. Appl. Phys.* **121** 033302
- [7] Winter J, Sousa J S, Sadeghi N, Schmidt-Bleker A, Reuter S and Puech V 2015 The spatio-temporal distribution of He (2^3S_1) metastable atoms in a MHz-driven helium plasma jet is influenced by the oxygen/nitrogen ratio of the surrounding atmosphere *Plasma Sources Sci. Technol.* **24** 025015
- [8] Reuter S, Winter J, Schmidt-Bleker A, Tresp H, Hammer M U and Weltmann K-D 2012 Controlling the ambient air affected reactive species composition in the effluent of an argon plasma jet *IEEE Trans. Plasma Sci.* **40** 2788–94
- [9] Reuter S, Von Woedtke T and Weltmann K D 2018 The kINPen - A review on physics and chemistry of the atmospheric pressure plasma jet and its applications *J. Phys. D: Appl. Phys.* **51** 233001
- [10] Nguyen T, Hernandez E, Donnelly V M and Economou D J 2018 Excitation mechanisms in a nonequilibrium helium plasma jet emerging in ambient air at 1 atm *J. Vac. Sci. Technol. A* **36** 04F406
- [11] Massines F, Gherardi N, Naudé N and Ségur P 2009 Recent advances in the understanding of homogeneous dielectric barrier discharges *Eur. Phys. J. Appl. Phys.* **47** 22805
- [12] Iseni S, Bruggeman P J, Weltmann K D and Reuter S 2016 Nitrogen metastable ($N_2(A^3\Sigma_u^+)$) in a cold argon atmospheric pressure plasma jet: shielding and gas composition *Appl. Phys. Lett.* **108** 184101
- [13] Schmidt-Bleker A, Winter J, Bösel A, Reuter S and Weltmann K D 2016 On the plasma chemistry of a cold atmospheric argon plasma jet with shielding gas device *Plasma Sources Sci. Technol.* **25** 015005
- [14] Yatom S, Luo Y, Xiong Q and Bruggeman P J 2017 Nanosecond pulsed humid Ar plasma jet in air: shielding, discharge characteristics and atomic hydrogen production *J. Phys. D: Appl. Phys.* **50** 415204
- [15] Jablonowski H, Hänsch M A C, Dünnbier M, Wende K, Hammer M U, Weltmann K-D, Reuter S and von Woedtke T 2015 Plasma jet's shielding gas impact on bacterial inactivation *Biointerphases* **10** 029506
- [16] Kapaldo J, Han X and Ptasinska S 2019 Shielding-gas-controlled atmospheric pressure plasma jets: optical emission, reactive oxygen species, and the effect on cancer cells *Plasma Process. Polym.* **16** 1800169
- [17] Tresp H, Hammer M U and Weltmann K 2013 Effects of atmosphere composition and liquid type on plasma-generated reactive species in biologically relevant solutions *Plasma Med.* **3** 45–55
- [18] Sigener F, Schäfer J, Weltmann K D, Foest R and Loffhagen D 2017 Modeling of a non-thermal RF plasma jet at atmospheric pressure *Plasma Process. Polym.* **14** 1600112
- [19] Babaeva N Y and Kushner M J 2014 Interaction of multiple atmospheric-pressure micro-plasma jets in small arrays: He/ O_2 into humid air *Plasma Sources Sci. Technol.* **23** 015007
- [20] Schmidt-Bleker A, Norberg S A, Winter J, Johnsen E, Reuter S, Weltmann K D and Kushner M J 2015

- Propagation mechanisms of guided streamers in plasma jets: the influence of electronegativity of the surrounding gas *Plasma Sources Sci. Technol.* **24** 035022
- [21] Hamilton J R et al 2017 QDB: a new database of plasma chemistries and reactions *Plasma Sources Sci. Technol.* **26** 055014
- [22] He_cross_section *Phelps database* (available at: <http://www.lxcat.net>) (Accessed March 1, 2018)
- [23] He*_cross_section *TRINITI database* (available at: <http://www.lxcat.net>) (Accessed March 1, 2018)
- [24] O₂_cross_section *TRINITI database* (available at: <http://www.lxcat.net>) (Accessed March 1, 2018)
- [25] Yan W and Economou D J 2016 Simulation of a non-equilibrium helium plasma bullet emerging into oxygen at high pressure (250–760 Torr) and interacting with a substrate *J. Appl. Phys.* **120** 123304
- [26] Breden D and Raja L L 2014 Computational study of the interaction of cold atmospheric helium plasma jets with surfaces *Plasma Sources Sci. Technol.* **23** 065020
- [27] Breden D, Miki K and Raja L L 2012 Self-consistent two-dimensional modeling of cold atmospheric-pressure plasma jets/bullets *Plasma Sources Sci. Technol.* **21** 034011
- [28] Breden D, Miki K and Raja L L 2011 Computational study of cold atmospheric nanosecond pulsed helium plasma jet in air *Appl. Phys. Lett.* **99** 111501
- [29] Lazarou C, Belmonte T, Chiper A S and Georghiou G E 2016 Numerical modelling of the effect of dry air traces in a helium parallel plate dielectric barrier discharge *Plasma Sources Sci. Technol.* **25** 055023
- [30] Liu X Y, Pei X K, Lu X P and Liu D W 2014 Numerical and experimental study on a pulsed-dc plasma jet *Plasma Sources Sci. Technol.* **23** 035007
- [31] Zhang P and Kortshagen U 2006 Two-dimensional numerical study of atmospheric pressure glows in helium with impurities *J. Phys. D: Appl. Phys.* **39** 153–63
- [32] Yan W and Economou D J 2017 Gas flow rate dependence of the discharge characteristics of a helium atmospheric pressure plasma jet interacting with a substrate *J. Phys. D: Appl. Phys.* **50** 415205
- [33] Stafford D S and Kushner M J 2004 O₂(¹Δ) production in He/O₂ mixtures in flowing low pressure plasmas *J. Appl. Phys.* **96** 2451–65
- [34] Murakami T, Niemi K, Gans T, O'Connell D and Graham W G 2013 Chemical kinetics and reactive species in atmospheric pressure helium-oxygen plasmas with humid-air impurities *Plasma Sources Sci. Technol.* **22** 015003
- [35] Castillo M, Méndez I, Islyaikin A M, Herrero V J and Tanarro I 2005 Low-pressure DC air plasmas. Investigation of neutral and ion chemistry *J. Phys. Chem. A* **109** 6255–63
- [36] Yuan X and Raja L L 2003 Computational study of capacitively coupled high-pressure glow discharges in helium *IEEE Trans. Plasma Sci.* **31** 495–503
- [37] Sakiyama Y, Graves D B, Chang H W, Shimizu T and Morfill G E 2012 Plasma chemistry model of surface microdischarge in humid air and dynamics of reactive neutral species *J. Phys. D: Appl. Phys.* **45** 425201
- [38] Pancheshnyi S, Nudnova M and Starikovskii A 2005 Development of a cathode-directed streamer discharge in air at different pressures: experiment and comparison with direct numerical simulation *Phys. Rev. E* **71** 016407
- [39] Atkinson R, Baulch D L, Cox R A, Hampson R F, Kerr J A, Rossi M J and Troe J 1997 Evaluated kinetic and photochemical data for atmospheric chemistry: supplement V. IUPAC Subcommittee on gas kinetic data evaluation for atmospheric chemistry *J. Phys. Chem. Ref. Data* **26** 521
- [40] Niemi K, Waskoenig J, Sadeghi N, Gans T and O'Connell D 2011 The role of helium metastable states in radio-frequency driven helium-oxygen atmospheric pressure plasma jets: measurement and numerical simulation *Plasma Sources Sci. Technol.* **20** 055005
- [41] Liu D X, Bruggeman P, Iza F, Rong M Z and Kong M G 2010 Global model of low-temperature atmospheric-pressure He + H₂O plasmas *Plasma Sources Sci. Technol.* **19** 025018
- [42] Kossyi I A, Kostinsky A Y, Matveyev A A and Silakov V P 1992 Kinetic scheme of the non-equilibrium discharge in nitrogen-oxygen mixtures *Plasma Sources Sci. Technol.* **1** 207–20
- [43] Sakiyama Y and Graves D B 2007 Nonthermal atmospheric rf plasma in one-dimensional spherical coordinates: asymmetric sheath structure and the discharge mechanism *J. Appl. Phys.* **101** 073306
- [44] Arakoni R A, Babaeva N Y and Kushner M J 2007 O₂(¹Δ) production and gain in plasma pumped oxygen-iodine lasers: consequences of NO and NO₂ additives *J. Phys. D: Appl. Phys.* **40** 4793–809
- [45] Van Laer K and Bogaerts A 2015 Fluid modelling of a packed bed dielectric barrier discharge plasma reactor *Plasma Sources Sci. Technol.* **25** 015002
- [46] Shao X J, Chang Z S, Mu H B, Liao W L and Zhang G J 2013 Experimental and numerical investigation on the interaction between air flow channel and air plasma jet at atmospheric pressure *IEEE Trans. Plasma Sci.* **41** 899–906
- [47] Hagelaar G J and Pitchford L C. 2005 Solving the Boltzmann equation to obtain electron transport coefficients and rate coefficients for fluid models *Plasma Sources Sci. Technol.* **14** 722–33
- [48] COMSOL 5.0 2014 (Burlington, MA: COMSOL)
- [49] Wang Q, Doll F, Donnelly V M, Economou D J, Sadeghi N and Franz G F 2007 Experimental and theoretical study of the effect of gas flow on gas temperature in an atmospheric pressure microplasma *J. Phys. D: Appl. Phys.* **40** 4202–11
- [50] Nguyen T, Lin P, Economou D and Donnelly V 2020 Optical emission self-actinometry method for measuring absolute number densities of air species diffusing into an atmospheric pressure helium plasma jet (submitted)
- [51] Lawler J E, Parker J W and Anderson L W 1979 Helium 3³S decay rates in a high-pressure afterglow *Phys. Rev. A* **19** 156–9
- [52] Hitachi A, King Terence A, Kubota S and Doke T 1980 Deexcitation of He Rydberg S and manifold states by N₂ *Phys. Rev. A* **22** 863–7
- [53] Filseth S V, Zia A and Welge K H 1970 Flash photolytic production, reactive lifetime, and collisional quenching of O₂(b¹Σ_g⁺, v'⁺=0) *J. Chem. Phys.* **52** 5502–10